Nano Research
https://doi.org/10.1007/s12274-017-1952-1
Research Article
ISSN 1998-0124
CN 11-5974/O4

Single-step flash-heat synthesis of red phosphorus/graphene flame-retardant composite as flexible anodes for sodium-ion batteries

Yihang Liu[1], Anyi Zhang[2], Chenfei Shen[2], Qingzhou Liu[2], Jiansong Cai[2], Xuan Cao[2], and Chongwu Zhou[1] (✉)

[1] *Ming Hsieh Department of Electrical Engineering, University of Southern California, Los Angeles, California 90089, USA*
[2] *Mork Family Department of Chemical Engineering and Materials Science, University of Southern California, Los Angeles, California 90089, USA*

Received: 6 September 2017
Revised: 18 October 2017
Accepted: 7 December 2017

KEYWORDS
sodium-ion batteries,
red phosphorus,
facile synthesis,
flexible,
flame-retardant,
reduced graphene oxide

ABSTRACT

Red phosphorus (RP) has attracted considerable attention as the anode for high-performance Na-ion batteries, owing to its low cost and high theoretical specific capacity of ~ 2,600 mAh/g. In this study, a facile single-step flash-heat treatment was developed to achieve the reduction of graphene oxide (GO) and the simultaneous deposition of RP onto the reduced graphene oxide (rGO) sheets. The resulting RP/rGO composite was shown to be a promising candidate for overcoming the issues associated with the poor electronic conductivity and large volume variation of RP during cycling. The RP/rGO flexible film anode delivered an average capacity of 1,625 mAh/g during 200 cycles at a charge/discharge current density of 1 A/g. Average charge capacities of 1,786, 1,597, 1,324, and 679 mAh/g at 1, 2, 4, and 6 A/g current densities were obtained in the rate capability tests. Moreover, owing to the RP component, the RP/rGO film presented superior flame retardancy compared to an rGO film. This work thus introduces a highly accessible synthesis method to prepare flexible and safe RP anodes with superior electrochemical performance toward Na-ion storage.

1 Introduction

Li-ion batteries have achieved considerable success as power sources of portable devices and electrical vehicles because of their superior specific energy density, Coulombic efficiency, and cycling stability [1, 2]. Na-ion batteries represent one of the main alternatives to the Li-ion ones, and have attracted increasing attention because of the abundance of sodium in both the earth's crust and the oceans [3–6]. Phosphorus plays a major role among various anode materials for Na-ion batteries, owing to its high theoretical specific capacity of ~ 2,600 mAh/g [7]. Despite the excellent performance of black P toward

Address correspondence to chongwuz@usc.edu

Na-ion storage [8–10], red P (RP) is the most cost-effective allotrope among phosphorus forms with adequate chemical stability for battery applications. Moreover, the incorporation of RP can potentially enhance the flame retardancy of the electrodes, because this material has been widely used as an effective flame retardant additive for decades [11]. However, micron-sized RP particles have been proven unsuitable for stable Na-ion storage, owing to their poor electronic conductivity and huge volume expansion during the sodiation process [12]. To produce nanosized RP, several studies utilizing the ball-milling technique with conductive materials such as carbon nanotubes, carbon nanofibers and graphene stacks have been reported [13–15]. Despite the encouraging improvements achieved in these studies, various complex issues ascribed to the simple mechanical mixing, such as the non-uniform particle size and the poor contact between the RP active material and the conductive platforms, still hamper the optimization of the electrochemical performance of RP anodes. Traditional vaporization–condensation methods, recently employed to prepare RP anodes, led to impressive performance enhancements relative to the micron-sized RP particles, owing to the uniform size of the RP particles and the good contact between the active material and the conductive scaffold [16–19]. However, the sophisticated synthetic processes involved in such methods, which involve sealing in quartz ampoules, introduce significant challenges associated with their productivity and scalability.

Herein, we report a facile flash-heat treatment to grow nanosized RP on the surface of reduced graphene oxide (rGO) sheets and in the void spaces between rGO layers; in particular, the RP deposition and GO reduction were completed simultaneously in a single-step heat treatment. The synthesis method of the RP/rGO composite is described schematically in Fig. 1. As shown in Fig. 1(a), the RP and GO precursors were arranged in a RP/GO/RP three-layer structure inside a ceramic boat with a ceramic cover, and then loaded in a tube furnace under Ar/H_2 atmosphere. The boat was initially placed on the side of the heating zone; after heating the furnace to 500 °C, the boat was moved into the heating zone, as shown in Fig. 1(b). As soon as P condensation was observed on a quartz tube placed downstream of the gas flow, the boat was immediately moved back to the original position, as illustrated in Fig. 1(c). Then, the boat was maintained at 300 °C for 6 h to convert white P to red P through a cooling-down process. The structure of the resulting RP/rGO composite, schematically shown in Fig. 1(d), combines several advantages: 1) Nanosized RP can shorten the ion diffusion length and thus enhance both ionic and electronic kinetics in the anode; 2) the RP particles occupy the gaps between the rGO sheets conformally, which protect them against volume variations during intercalation and extraction of Na ions; 3) the rGO network can provide an electron pathway and thus increase the electronic conductivity of the RP anode. Furthermore, the flash-heat treatment process reported here is simpler and more cost-effective than the traditional ball-milling and vaporization–

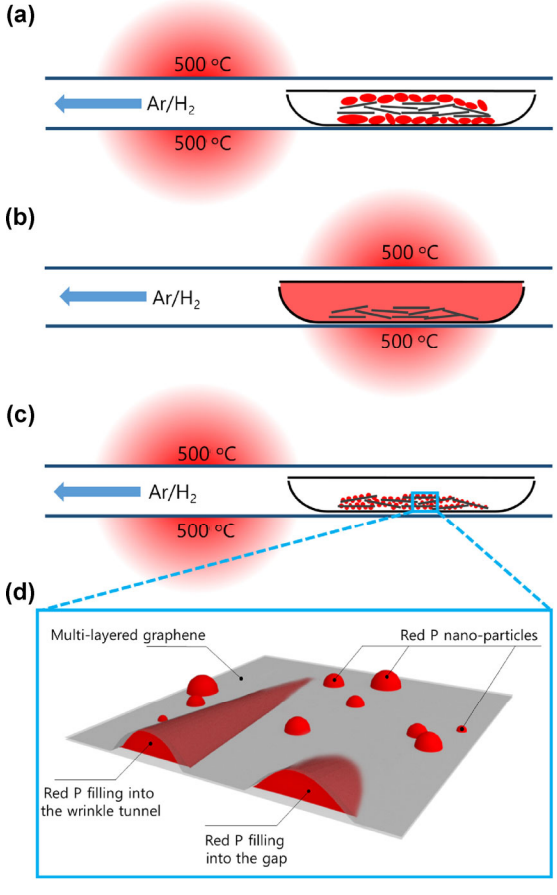

Figure 1 Schematic diagrams of the synthesis process of the RP/rGO composite: (a) pre-heat treatment; (b) flash-heat treatment; (c) cooling-down stage. (d) Schematic illustration of the nanostructure of the resulting RP/rGO composite.

condensation methods, and thus enables the large-throughput manufacturing of RP anodes [20, 21].

2 Experimental

2.1 Materials preparation

To synthesize the RP/rGO composite, the RP precursor was initially dried at 90 °C to remove moisture and then filtered with a 30 μm mesh. The RP and GO powder precursors were arranged in a RP/GO/RP three-layer structure inside a ceramic boat with a ceramic cover. The boat was loaded into a tube furnace under Ar/H_2 flow (5% H_2), and initially placed on the side of the heating zone. After heating the furnace to 500 °C, the boat was moved into the heating zone; as soon as P condensation was observed on the inner surface of a quartz tube located downstream of the gas flow (~ 1 min), the boat was immediately moved back to the original position. Then, the temperature of the boat was maintained at 300 °C for 6 h, to convert white P to red P. After a cooling-down process, the resulting RP/rGO composite was transferred into an Ar-filled glovebox, washed with methanol, and dried. The preparation of the rGO and P-treated rGO control samples and the fabrication of the flexible film electrode are described in the Electronic Supplementary Material (ESM).

2.2 Materials characterization

Surface morphology and energy-dispersive X-ray spectroscopy (EDS) measurements were performed with a JEOL JSM-7001 microscope operating at 15 kV, the samples were assembled onto the specimen by carbon tapes. Field-emission transmission electron microscopy (TEM, JEOL JEM 2100F, 200 kV) was employed to obtain TEM and scanning transmission electron microscopy (STEM) images, along with EDS profiles. The samples were first dispersed in ethanol through ultrasonication and then collected using carbon film-covered copper grids for the analysis. Thermogravimetric analysis (TGA) measurements were carried out using a Netzsch STA instrument at a heating rate of 1 °C/min under N_2 atmosphere, in a temperature range from room temperature to 800 °C. Raman spectra were recorded using a Renishaw InVia spectrometer with a 532 nm laser (10 μW) focused through a 100× objective lens. Raman spectra were collected at room temperature under ambient conditions, using glass slides as substrates to carry the powder samples.

2.3 Electrochemical measurements

Electrochemical tests were conducted in CR2032 coin cells, with Na metal as counter electrode and 1 M $NaClO_4$ in dimethyl carbonate (DMC) electrolyte with 10% (v/v) fluoroethylene carbonate (FEC) as additive, to form a strong and stable solid electrolyte interface (SEI) film in the first cycle. A RP/rGO film with a thickness of ~ 110 μm was cut into electrodes with a diameter of 16 mm for the electrochemical tests, and the mass of each electrode was ~ 1.2 mg. All batteries were assembled inside an argon-filled glovebox with water and oxygen contents below 0.1 ppm. To prepare commercial RP control anodes mixed with rGO and carbon black (CB), RP powder was mixed with polyvinylidene fluoride (PVDF) in 1-methyl-2-pyrrolidinone (NMP) and rGO or CB in a weight ratio of 50:10:40, using high energy ball milling for 1 h in an argon-filled ball-mill jar. The resulting slurry was cast onto an Al foil, dried at 90 °C in air overnight, and then punched into electrodes with the size of CR2032-type cells. The mass loading of active material on the Al foil current collector was ~ 1.5 mg/cm^2. In the cycling stability and rate capability tests, batteries were cycled in the voltage range from 0.01 to 1.75 V vs. Na/Na^+ at room temperature. All capacities and current densities were calculated based on the mass of RP only, unless noted otherwise.

3 Results and discussion

The scanning electron microscopy (SEM), TEM, and STEM images of the as-produced RP/rGO composite, discussed below, show the presence of RP nanodots deposited on the rGO surface and of aggregates of nanosized RP in the void spaces between rGO layers. The SEM images of the RP/rGO composite at different magnifications, shown in Figs. 2(a) and 2(b), highlight the dense and uniform distribution of the nanosized P particles grown on the rGO sheets. Figures 2(c) and 2(d) show the TEM and STEM images, respectively, of a portion of RP/rGO flake, confirming the presence

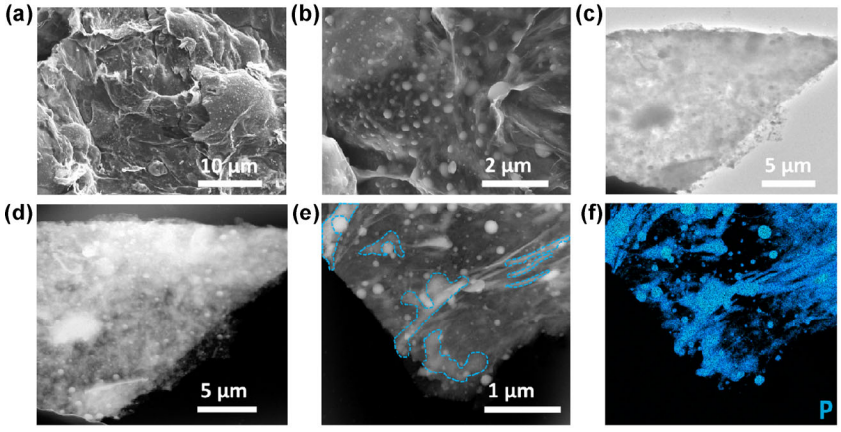

Figure 2 (a) and (b) SEM images of the RP/rGO composite at (a) 1,500× and (b) 4,000× magnification. (c) and (d) TEM and STEM images of a single piece of RP/rGO flake. (e) Enlarged STEM image of the RP/rGO composite, with corresponding EDS mapping profile of P element shown in (f). The RP particles occupying the void spaces between the rGO layers are marked by blue lines in (e).

of P nanoparticles of morphology consistent with the SEM images. Dense growth of RP particles can be easily observed in the dark-field STEM image shown in Fig. 2(d), based on the sharp contrast difference between P and rGO. To further confirm the uniformity of the present samples, additional SEM and TEM images are displayed in Figs. S1 and S2 in the ESM. Figure S2(c) in the ESM shows a high-resolution TEM image taken at the edge of a single piece of RP/rGO sheet, with blue dashed lines indicating multilayered rGO. Further details of the architectural structure of the RP/rGO composite can be obtained from the enlarged STEM image shown in Fig. 2(e), whereas the corresponding EDS mapping of P element is displayed in Fig. 2(f): Besides the nanosized P particles deposited on the surface, considerable amounts of P occupy the void spaces between rGO layers through gaps and wrinkle tunnels (marked by blue dashed lines in Fig. 2(e)), indicating conformal protection of the P particles by the strong rGO layers. The TGA profiles of the RP/rGO composite and of an rGO control sample in nitrogen atmosphere are shown in Fig. S3 in the ESM. The synthesized RP/rGO composite exhibits a sharp weight loss between 400 and 450 °C due to the vaporization of RP, and the weight percentage of RP in the composite was calculated as 57.9%.

The Raman spectra of the RP/rGO composite and of commercial RP powder are displayed in Fig. 3(a). Besides the D and G bands peaking at 1,331 and 1,577 cm^{-1}, the spectrum of the RP/rGO composite contains a small broad 2D band, indicating the multilayered nature of the rGO sheets. Compared to the commercial RP sample, the RP signal was also detected between 300 and 500 cm^{-1} in the Raman spectrum of the synthesized RP/rGO composite, indicating that the P domains observed in Fig. 2 correspond to the RP form. The XRD patterns of the GO, RP, and RP/rGO samples are shown in Fig. S4 in the ESM. The GO precursor shows a major (002) peak at ~ 10°, which disappears after the flash-heat treatment, indicating the successful reduction of GO. Figure 3(b) displays the X-ray photoelectron spectroscopy (XPS) spectrum of the RP/rGO composite and of the pristine GO used as precursor in the RP/rGO synthesis. Both 2p and 2s peaks of phosphorus are detected in the spectrum of the RP/rGO composite, while the intensity of the O 1s peak is considerable reduced compared to the GO sample, indicating that most of the oxygen-containing functional groups were eliminated during the heat-treatment process. Further details on the reduction of GO can be obtained from Fig. 3(c), which shows the C 1s high-resolution XPS spectrum of the two samples. The spectrum of the pristine GO sample can be fitted with three Gaussian–Lorentzian peaks at 284.6, 286.3, and 287.2 eV, corresponding to C=C/C–C, C–O, and O–C=O bonds, respectively. The spectrum of the RP/rGO composite shows peaks at 284.5 and 285.6 eV, corresponding to C=C/C–C and C–O bonds, respectively. Compared with the GO sample, the intensity of the C–O peak of the RP/rGO composite

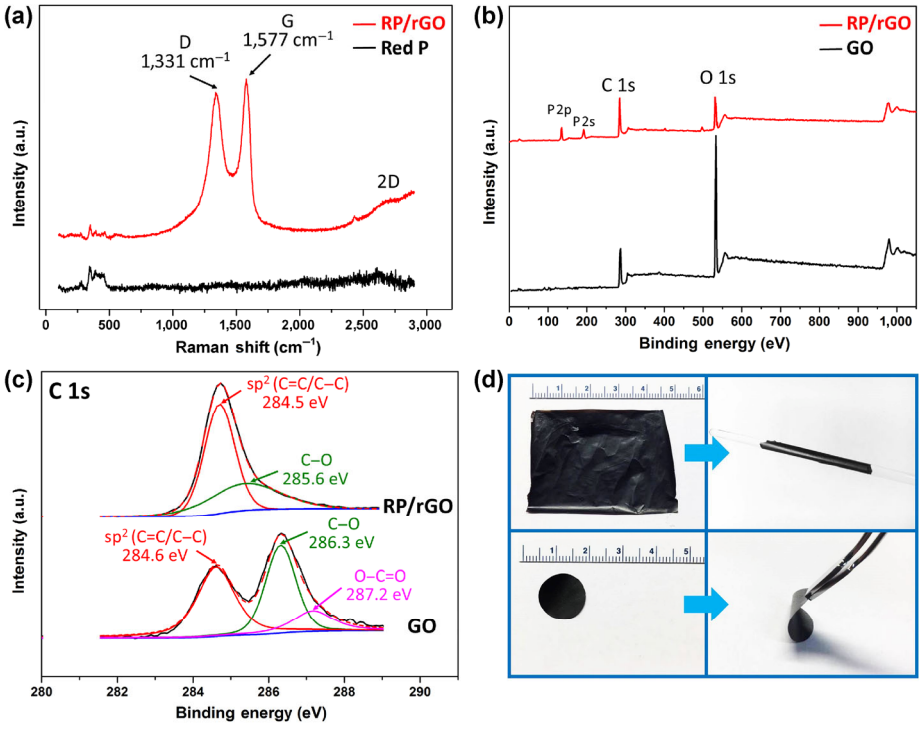

Figure 3 (a) Raman spectra of RP/rGO composite and commercial RP powder. (b) XPS spectrum of synthesized RP/rGO composite and pristine GO powder. (c) High-resolution C 1s XPS spectrum of synthesized RP/rGO composite and pristine GO powder. (d) Optical images of a flexible RP/rGO film wrapped on a glass rod with a diameter of 5 mm, and of a punched electrode bent with a pair of tweezers.

is markedly reduced and the O–C=O peak almost vanishes, indicating that GO was thermally reduced during the heattreatment used to synthesize the RP/rGO composite in Ar/H_2 atmosphere [22–24]. No obvious C–P bond signal was detected in the Raman and XPS spectra of the RP/rGO composite, implying that the heating temperature might be too low and/or the heating time might be too short to achieve a relatively high P-doping concentration in graphene during the synthesis process [25]. The O 1s high-resolution spectra of the two samples shown in Fig. S5 in the ESM also confirm the thermal reduction of GO, as the 531.7 eV signal corresponding to the O=C bond of the GO sample disappeared after the heat treatment, and only the peak of the O–C bond at 533.1 eV was observed for the RP/rGO composite. The synthesized RP/rGO composite can be easily fabricated into highly flexible free-standing films through a filtration method, as shown in the optical images of Fig. 3(d), with additional details reported in the ESM. No visible fractures were detected in the film during bending on a glass rod with a diameter of 5 mm. The film was then punched into electrodes with a diameter of 17 mm for the electrochemical performance tests described below.

The electrochemical performances of the RP/rGO composite and the commercial RP control sample were first investigated by galvanostatic charge/discharge cycling experiments between 0.01 and 1.75 V at a current density of 1 A/g and with Na metal as counter electrode, as shown in Fig. 4(a). As no obvious doping by P heteroatoms was detected in rGO, and the rGO network worked as current collector in the RP/rGO free-standing electrode, all current densities and capacities were calculated based on the mass of RP only, unless noted otherwise. Specific charge capacities of 2,197 and 1,883 mAh/g were observed in the first and second cycle, respectively. Afterward, the capacity showed a slight increase from 1,705 to 1,823 mAh/g from the 3rd to the 50th cycle, and then became stabilized at ~ 1,550 mAh/g between the 50th and the 200th cycle. In contrast, commercial RP mixed with rGO and CB delivered similar initial capacities, but suffered from a rapid capacity fading during the

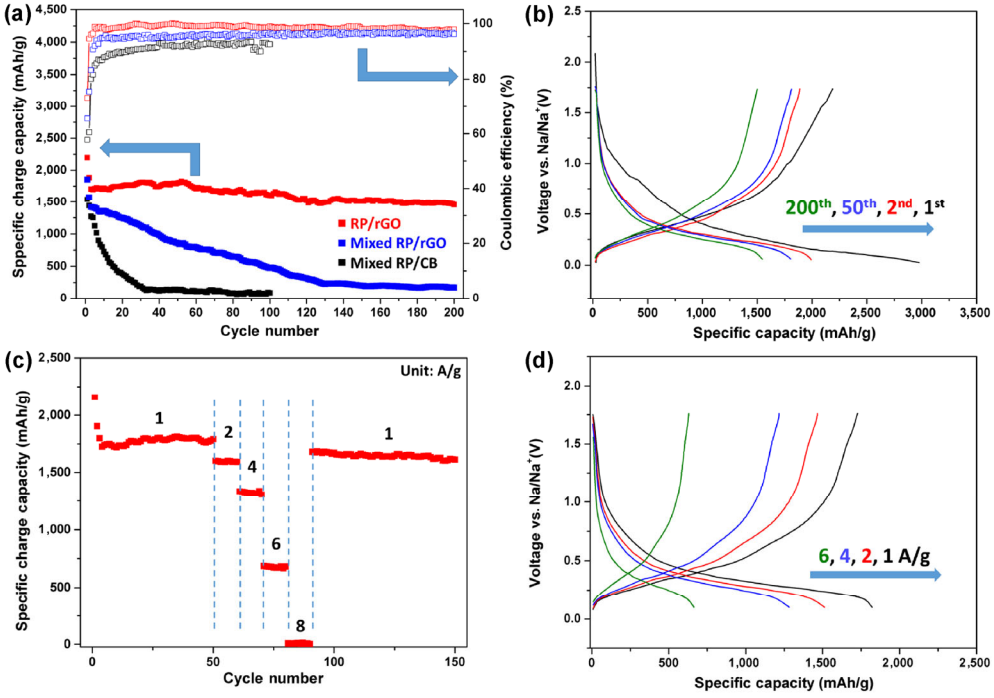

Figure 4 (a) Cycling performance of fabricated RP/rGO flexible film anode, commercial RP mixed with rGO, and commercial RP mixed with CB at a charge/discharge current density of 1 A/g, with corresponding potential profiles shown in (b). Rate performance of the RP/rGO anode, with potential profiles shown in (d).

first 30 and 120 cycles. Thus, the cycling stability of the RP/rGO anode was significantly enhanced by the deposition of nanosized RP particles on the surface of rGO sheets and within the void spaces between rGO layers; in addition, the architectural rGO structure provided a conductive supporting network with superior mechanical properties.

The RP/rGO film electrode exhibited a 73.2% efficiency at the first cycle, which rapidly increased to ~ 98% after five cycles. Similar to silicon anodes for lithium-ion batteries, the relatively low initial efficiency may derive from Na consumption during SEI formation on the surface of RP particles deposited on graphene sheets without the conformal coating protection from graphene. The low initial Coulombic efficiency can represent a problem for practical applications of the RP anodes. However, methods such as pre-sodiation and artificial SEI film coating can be adopted to overcome this issue [26, 27].

In order to determine the capacity contribution from the rGO with P heteroatom-doping, the cycling performance of the untreated rGO and P-treated rGO control samples are presented in Fig. S6(a) in the ESM, while representative charge/discharge curves are shown in Fig. S6(b) in the ESM, and the details on the synthesis of the two control samples are reported in the ESM. The untreated and P-treated rGO samples deliver average specific charge capacities of 47 and 67 mAh/g, respectively, during 50 cycles at a 100 mA/g current density. The limited capacity increase of the P-treated rGO sample relative to the untreated rGO sample indicates that the P dopant concentration in graphene is relatively low, in good agreement with the XPS data presented in Fig. 3(d). This finding also implies that the P-doped rGO gives only a minor contribution to the capacity of the synthesized RP/rGO composite [28, 29]. Figure 4(a) shows that the RP/rGO flexible film anode achieved an average capacity of 1,625 mAh/g during 200 cycles at 1 A/g charge/discharge current density, which would decrease to 941 mAh/g if calculated based on the total mass of the free-standing electrode. The capacity of the present free-standing RP/rGO film electrode during long cycling tests is comparable to that of silicon anodes employed in lithium-ion batteries containing conductive carbon and binder additives in 15%–20% weight ratio, and becomes

actually higher if we take into account the weight of the copper foil used as anode current collector in traditional battery cells [30–32].

In addition to the capacity, the voltage profiles provide further details about the electrochemical sodiation/de-sodiation process in the present anodes. The voltage profiles corresponding to the cycling performance test of the RP/rGO anode are shown in Fig. 4(b), with cycle numbers labeled on the side. A small potential plateau at 0.7 V and the main sodiation plateau between 0.5 and 0.1 V were observed during the first sodiation process. The minor plateau at 0.7 V is due to the formation of the SEI film caused by the decomposition of the electrolyte, which contributes to the irreversible capacity in the first cycle. The disappearance of this plateau in the following cycles indicates that a stable SEI film was formed. The discharge curves at the 2nd, 50th, and 200th cycle consistently present a main plateau at 0.4–0.1 V. All charge curves exhibit a main de-sodiation plateau at 0.2–0.7 V.

Figure 4(c) shows the results of the rate capability tests performed with charge/discharge current densities ranging from 1 to 8 A/g. The anode delivered average capacities of 1,786, 1,597, 1,324, and 679 mAh/g at current densities of 1, 2, 4, and 6 A/g, respectively, while a capacity of ~ 10 mAh/g was observed at the current density of 8 A/g. The anode retained a capacity of ~ 1,640 mAh/g upon switching the current density back to 1 A/g after 90 cycles. Representative charge/discharge curves at different current densities are shown in Fig. 4(d). The enlarged hysteresis between the charge and discharge curves was attributed to the higher current densities, and the main sodiation and de-sodiation plateaus were located at 0.1–0.4 and 0.2–0.7 V for all curves. The superior rate performance discussed above can be attributed to the significant enhancement in the sodium ion transport kinetics due to the nanosized RP, and to the improved rate capability of the whole electrode associated with the excellent electronic conductance of the architectural rGO network serving as electron pathway.

To gain insight into the structural changes in the RP/rGO anode during long-term cycling, TEM images and the corresponding EDS elemental mappings of the electrode were collected after 200 cycles in a fully sodiated status, as shown in Fig. 5. Before the analysis, the post-cycling electrode was immersed in electrolyte solvent overnight to remove the Na salt. The use of $NaClO_4$ as the sodium conducting salt in this study rules out P signals originating from the electrolyte salt, as in the case of $NaPF_6$. The post-cycling TEM and STEM images of a single piece of the RP/rGO composite are shown in Figs. 5(a) and 5(b). The corresponding EDS spectrum is presented in Fig. 5(c), while the elemental mappings are presented in Figs. 5(d)–5(f) for carbon, sodium, and phosphorus, respectively. The elemental mapping profile of phosphorus shows the presence of an RP flake of micrometer size attached to the graphene sheet, indicating that agglomeration of RP nanosized particles took place on the surface of rGO sheets during cycling. The mapping profiles of three elements reached a good coincidence, which implies that most of the active RP material survived during the 200 cycles performed, and that the architectural structure of RP/rGO is suitable for long-term cycling.

Although the batteries have achieved considerable success in both academic and industrial fields, safety risks associated with the use of highly flammable liquid organic electrolytes remain a critical issue [33–35]. Many strategies have been explored to overcome this problem, such as the development of non-flammable electrolytes [36–39], the addition of flame-retardant additives to the electrolyte [40–43], and separator engineering approaches [44–46]. The flame retardancy of the electrodes is one of the key factors for the design of safer batteries, as it may prevent flame spreading after ignition of the electrolyte. Since RP has been one of the most widely used fire retardants over the past several decades [11], the flame retardancy of the RP/rGO composite was investigated by combustion tests comparing the performance of the RP/rGO film and a control rGO film. Both films were immersed in the electrolyte solvent for 3 h before the tests. The optical images corresponding to the tests at t = 0, 0.5, 2, 5, and 10 s are presented in Figs. 6(a) and 6(b) for the RP/rGO and rGO films, respectively; t = 0 s is defined as the time when the flame can be clearly observed on the films. The flame was fully developed at 0.5 s, with red-hot edges formed on both films due

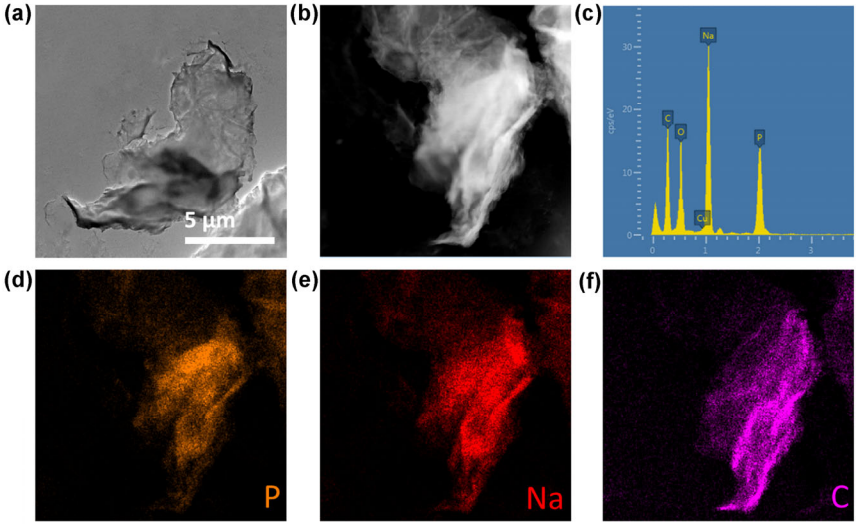

Figure 5 (a) and (b) TEM and STEM images of the flexible RP/rGO anode after 200 cycles, with corresponding EDS spectrum (c) and elemental mapping profiles of phosphorus (d), sodium (e), and carbon (f).

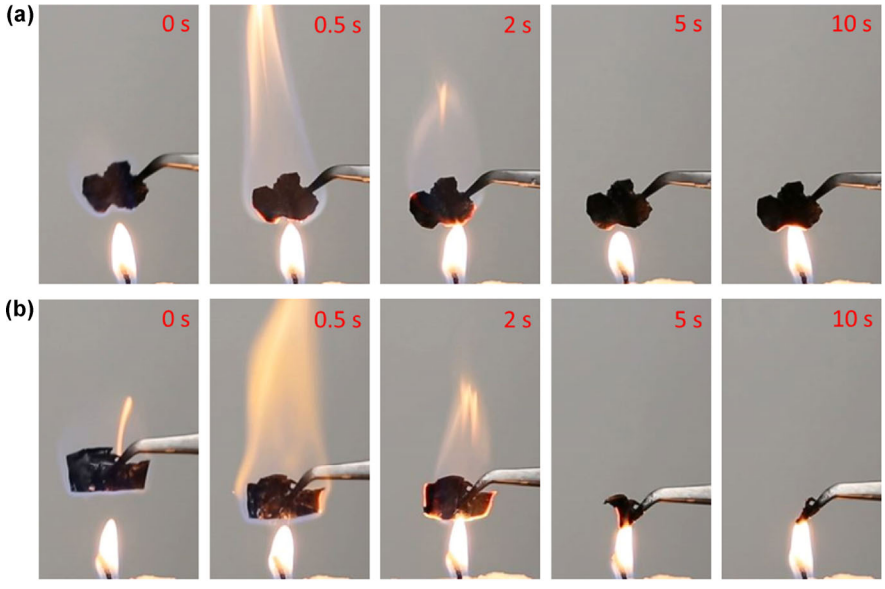

Figure 6 Combustion tests of RP/rGO flexible film (a) and rGO film (b) at t = 0, 0.5, 2, 5, and 10 s; t = 0 s is defined as the time when the flame can be clearly observed on the films.

to the combustion of the electrolyte. Afterward, the flame was attenuated due to exhaustion of the electrolyte on the surface of (and absorbed by) the films. Most of the rGO film was burned out from 5 to 10 s, with the red-hot edge moving inward. On the other hand, the red-hot edge of the RP/rGO film vanished at ~ 5 s, and only a small portion of the film was burned out between 5 and 10 s. Videos of the combustion tests can be found in the ESM. The RP/rGO film achieved excellent flame retardancy because of the formation of a phosphoric acid derivative, which can isolate the burning material from oxygen and catalyze char layer formation on the material surface, further preventing flame formation [47, 48].

4 Conclusions

In summary, we have developed a single-step flash-heat treatment to deposit nanosized RP on the surface of rGO sheets and in the void spaces between

rGO layers. Both the RP growth and GO reduction were completed within the single-step flash-heat treatment. The nanosized RP not only reduced the internal stress during sodiation/de-sodiation, leading to long cycle life, but also decreased the sodium ion diffusion length, enhancing the transport kinetics. The RP anode exhibited improved electrochemical performance, owing to the rGO network that served as electron pathway and provided excellent mechanical support to the RP particles in the void spaces between rGO layers against volume variations during cycling. The resulting RP/rGO flexible anode delivered specific charge capacities of 1,786, 1,597, 1,324, and 679 mAh/g at charge/discharge current densities of 1, 2, 4, and 6 A/g, and an average capacity of 1,625 mAh/g during 200 deep cycles at 1 A/g, which would convert to 941 mAh/g if it was calculated based on the total mass of the free-standing RP/rGO film electrode. Moreover, the RP/rGO film also obtained excellent flame retardancy by taking advantage of the RP ingredient. The superior electrochemical performances of the RP/rGO flexible film electrode, combined with its improved flame retardancy, highlight the considerable potential of these systems for the development of inexpensive, safe, and wearable Na-based energy storage devices.

Acknowledgements

We would like to acknowledge the collaboration of this research with King Abdul-Aziz City for Science and Technology (KACST) via The Center of Excellence for Nanotechnologies (CEGN). A portion of the images and data used in this article were acquired at The Center for Electron Microscopy and Microanalysis, University of Southern California.

Electronic Supplementary Material: Supplementary material (the preparation of rGO and P-treated rGO, the fabrication details of the flexible film electrodes, the additional SEM, TEM and STEM images, the TGA results, the XPS analysis, the electrochemical tests of the rGO and P-treated rGO control samples, and the videos of the combustion tests) is available in the online version of this article at https://doi.org/10.1007/s12274-017-1952-1.

References

[1] Bruce, P. G.; Scrosati, B.; Tarascon, J. M. Nanomaterials for rechargeable lithium batteries. *Angew. Chem., Int. Ed.* **2008**, *47*, 2930–2946.

[2] Li, H.; Wang, Z. X.; Chen, L. Q.; Huang, X. J. Research on advanced materials for Li-ion batteries. *Adv. Mater.* **2009**, *21*, 4593–4607.

[3] Luo, W.; Shen, F.; Bommier, C.; Zhu, H. L.; Ji, X. L.; Hu, L. B. Na-ion battery anodes: Materials and electrochemistry. *Acc. Chem. Res.* **2016**, *49*, 231–240.

[4] Kundu, D.; Talaie, E.; Duffort, V.; Nazar, L. F. The emerging chemistry of sodium ion batteries for electrochemical energy storage. *Angew. Chem., Int. Ed.* **2015**, *54*, 3431–3448.

[5] Liu, Y. H.; Fang, X.; Ge, M. Y.; Rong, J. P.; Shen, C. F.; Zhang, A. Y.; Enaya, H. A.; Zhou, C. W. SnO_2 coated carbon cloth with surface modification as Na-ion battery anode. *Nano Energy* **2015**, *16*, 399–407.

[6] Liu, Y. H.; Fang, X.; Zhang, A. Y.; Shen, C. F.; Liu, Q. Z.; Enaya, H. A.; Zhou, C. W. Layered P2-$Na_{2/3}[Ni_{1/3}Mn_{2/3}]O_2$ as high-voltage cathode for sodium-ion batteries: The capacity decay mechanism and Al_2O_3 surface modification. *Nano Energy* **2016**, *27*, 27–34.

[7] Yabuuchi, N.; Kubota, K.; Dahbi, M.; Komaba, S. Research development on sodium-ion batteries. *Chem. Rev.* **2014**, *114*, 11636–11682.

[8] Peng, Q.; Hu, K. M.; Sa, B. S.; Zhou, J.; Wu, B.; Hou, X. H.; Sun, Z. M. Unexpected elastic isotropy in a black phosphorene/TiC_2 van der Waals heterostructure with flexible Li-ion battery anode applications. *Nano Res.* **2017**, *10*, 3136–3150.

[9] Xu, G. L.; Chen, Z. H.; Zhong, G. M.; Liu, Y. Z.; Yang, Y.; Ma, T. Y.; Ren, Y.; Zhou, X. B.; Wu, X. H.; Zhang, X. Y. et al. Nanostructured black phosphorus/ketjenblack-multiwalled carbon nanotubes composite as high performance anode material for sodium-ion batteries. *Nano Lett.* **2016**, *16*, 3955–3965.

[10] Chen, L.; Zhou, G. M.; Liu, Z. B.; Ma, X. M.; Chen, J.; Zhang, Z. Y.; Ma, X. L.; Li, F.; Cheng, H. M.; Ren, W. C. Scalable clean exfoliation of high-quality few-layer black phosphorus for a flexible lithium ion battery. *Adv. Mater.* **2016**, *28*, 510–517.

[11] Levchik, S. V.; Weil, E. D. A review of recent progress in phosphorus-based flame retardants. *J. Fire Sci.* **2006**, *24*, 345–364.

[12] Li, W. J.; Chou, S. L.; Wang, J. Z.; Liu, H. K.; Dou, S. X. Simply mixed commercial red phosphorus and carbon nanotube composite with exceptionally reversible sodium-ion storage. *Nano Lett.* **2013**, *13*, 5480–5484.

[13] Kim, Y.; Park, Y.; Choi, A.; Choi, N. S.; Kim, J.; Lee, J.; Ryu, J. H.; Oh, S. M.; Lee, K. T. An amorphous red phosphorus/carbon composite as a promising anode material for sodium ion batteries. *Adv. Mater.* **2013**, *25*, 3045–3049.

[14] Qian, J. F.; Wu, X. Y.; Cao, Y. L.; Ai, X. P.; Yang, H. X. High capacity and rate capability of amorphous phosphorus for sodium ion batteries. *Angew. Chem.* **2013**, *125*, 4731–4734.

[15] Song, J. X.; Yu, Z. X.; Gordin, M. L.; Hu, S.; Yi, R.; Tang, D. H.; Walter, T.; Regula, M.; Choi, D.; Li, X. L. et al. Chemically bonded phosphorus/graphene hybrid as a high performance anode for sodium-ion batteries. *Nano Lett.* **2014**, *14*, 6329–6335.

[16] Zhang, C.; Wang, X.; Liang, Q. F.; Liu, X. Z.; Weng, Q. H.; Liu, J. W.; Yang, Y. J.; Dai, Z. H.; Ding, K. J.; Bando, Y. et al. Amorphous phosphorus/nitrogen-doped graphene paper for ultrastable sodium-ion batteries. *Nano Lett.* **2016**, *16*, 2054–2060.

[17] Liu, Y. H.; Zhang, A. Y.; Shen, C. F.; Liu, Q. Z.; Cao, X.; Ma, Y. Q.; Chen, L.; Lau, C.; Chen, T. C.; Wei, F. W. et al. Red phosphorus nanodots on reduced graphene oxide as a flexible and ultra-fast anode for sodium-ion batteries. *ACS Nano* **2017**, *11*, 5530–5537.

[18] Li, W. H.; Yang, Z. Z.; Li, M. S.; Jiang, Y.; Wei, X.; Zhong, X. W.; Gu, L.; Yu, Y. Amorphous red phosphorus embedded in highly ordered mesoporous carbon with superior lithium and sodium storage capacity. *Nano Lett.* **2016**, *16*, 1546–1553.

[19] Li, W. H.; Hu, S. H.; Luo, X. Y.; Li, Z. L.; Sun, X. Z.; Li, M. S.; Liu, F. F.; Yu, Y. Confined amorphous red phosphorus in MOF-derived N-doped microporous carbon as a superior anode for sodium-ion battery. *Adv. Mater.* **2017**, *29*, 1605820.

[20] Chen, Y. N.; Egan, G. C.; Wan, J. Y.; Zhu, S. Z.; Jacob, R. J.; Zhou, W. B.; Dai, J. Q.; Wang, Y. B.; Danner, V. A.; Yao, Y. G. et al. Ultra-fast self-assembly and stabilization of reactive nanoparticles in reduced graphene oxide films. *Nat. Commun.* **2016**, *7*, 12332.

[21] Yao, Y. G.; Chen, F. J.; Nie, A. M.; Lacey, S. D.; Jacob, R. J.; Xu, S. M.; Huang, Z. N.; Fu, K.; Dai, J. Q.; Salamanca-Riba, L. et al. *In situ* high temperature synthesis of single-component metallic nanoparticles. *ACS Cent. Sci.* **2017**, *3*, 294–301.

[22] Dave, K.; Park, K. H.; Dhayal, M. Two-step process for programmable removal of oxygen functionalities of graphene oxide: Functional, structural and electrical characteristics. *RSC Adv.* **2015**, *5*, 95657–95665.

[23] Penmatsa, V.; Kim, T.; Beidaghi, M.; Kawarada, H.; Gu, L.; Wang, Z. F.; Wang, C. L. Three-dimensional graphene nanosheet encrusted carbon micropillar arrays for electrochemical sensing. *Nanoscale* **2012**, *4*, 3673–3678.

[24] Dreyer, D. R.; Park, S.; Bielawski, C. W.; Ruoff, R. S. The chemistry of graphene oxide. *Chem. Soc. Rev.* **2010**, *39*, 228–240.

[25] Sun, J.; Zheng, G. Y.; Lee, H.-W.; Liu, N.; Wang, H. T.; Yao, H. B.; Yang, W. S.; Cui, Y. Formation of stable phosphorus-carbon bond for enhanced performance in black phosphorus nanoparticle-graphite composite battery anodes. *Nano Lett.* **2014**, *14*, 4573–4580.

[26] Forney, M. W.; Ganter, M. J.; Staub, J. W.; Ridgley, R. D.; Landi, B. J. Prelithiation of silicon-carbon nanotube anodes for lithium ion batteries by stabilized lithium metal powder (SLMP). *Nano Lett.* **2013**, *13*, 4158–4163.

[27] Zhao, J.; Lu, Z. D.; Wang, H. T.; Liu, W.; Lee, H. W.; Yan, K.; Zhou, D.; Lin, D. C.; Liu, N.; Cui, Y. Artificial solid electrolyte interphase-protected Li_xSi nanoparticles: An efficient and stable prelithiation reagent for lithium-ion batteries. *J. Am. Chem. Soc.* **2015**, *137*, 8372–8375.

[28] Yang, Y. J.; Tang, D.-M.; Zhang, C.; Zhang, Y. H.; Liang, Q. F.; Chen, S. M.; Weng, Q. H.; Zhou, M.; Xue, Y. M.; Liu, J. W. et al. "Protrusions" or "holes" in graphene: Which is the better choice for sodium ion storage? *Energy Environ. Sci.* **2017**, *10*, 979–986.

[29] Ma, G. Y.; Xiang, Z. H.; Huang, K. S.; Ju, Z. C.; Zhuang, Q. C.; Cui, Y. H. Graphene-based phosphorus-doped carbon as anode material for high-performance sodium-ion batteries. *Part. Part. Syst. Charact.* **2017**, *34*, 1600315.

[30] Lu, L. G.; Han, X. B.; Li, J. Q.; Hua, J. F.; Ouyang, M. G. A review on the key issues for lithium-ion battery management in electric vehicles. *J. Power Sources* **2013**, *226*, 272–288.

[31] Zong, L. Q.; Zhu, B.; Lu, Z. D.; Tan, Y. L.; Jin, Y.; Liu, N.; Hu, Y.; Gu, S.; Zhu, J.; Cui, Y. Nanopurification of silicon from 84% to 99.999% purity with a simple and scalable process. *Proc. Natl. Acad. Sci. USA* **2015**, *112*, 13473–13477.

[32] Zhu, B.; Jin, Y.; Tan, Y. L.; Zong, L. Q.; Hu, Y.; Chen, L.; Chen, Y. B.; Zhang, Q.; Zhu, J. Scalable production of Si nanoparticles directly from low grade sources for lithium-ion battery anode. *Nano Lett.* **2015**, *15*, 5750–5754.

[33] Luo, W.; Wang, Y. X.; Wang, L. J.; Jiang, W.; Chou, S.-L.; Dou, S. X.; Liu, H. K.; Yang, J. P. Silicon/mesoporous carbon/crystalline TiO_2 nanoparticles for highly stable lithium storage. *ACS Nano* **2016**, *10*, 10524–10532.

[34] Balakrishnan, P. G.; Ramesh, R.; Kumar, T. P. Safety mechanisms in lithium-ion batteries. *J. Power Sources* **2006**, *155*, 401–414.

[35] Janek, J.; Zeier, W. G. A solid future for battery development. *Nat. Energy* **2016**, *1*, 16141.

[36] Xu, K. Nonaqueous liquid electrolytes for lithium-based rechargeable batteries. *Chem. Rev.* **2004**, *104*, 4303–4418.

[37] Zhang, S. S. A review on electrolyte additives for lithium-ion batteries. *J. Power Sources* **2006**, *162*, 1379–1394.

[38] Nakagawa, H.; Fujino, Y.; Kozono, S.; Katayama, Y.; Nukuda, T.; Sakaebe, H.; Matsumoto, H.; Tatsumi, K. Application of nonflammable electrolyte with room temperature ionic liquids (RTILs) for lithium-ion cells. *J. Power Sources* **2007**, *174*, 1021–1026.

[39] Xu, K.; Ding, M. S.; Zhang, S. S.; Allen, J. L.; Jow, T. R. An attempt to formulate nonflammable lithium ion electrolytes with alkyl phosphates and phosphazenes. *J. Electrochem. Soc.* **2002**, *149*, A622–A626.

[40] Hyung, Y. E.; Vissers, D. R.; Amine, K. Flame-retardant additives for lithium-ion batteries. *J. Power Sources* **2003**, *119–121*, 383–387.

[41] Xiang, H. F.; Xu, H. Y.; Wang, Z. Z.; Chen, C. H. Dimethyl methylphosphonate (DMMP) as an efficient flame retardant additive for the lithium-ion battery electrolytes. *J. Power Sources* **2007**, *173*, 562–564.

[42] Shim, E. G.; Nam, T. H.; Kim, J. G.; Kim, H. S.; Moon, S. I. Diphenyloctyl phosphate as a flame-retardant additive in electrolyte for Li-ion batteries. *J. Power Sources* 2008, *175*, 533–539.

[43] Zhu, X. M.; Jiang, X. Y.; Ai, X. P.; Yang, H. X.; Cao, Y. L. Bis(2,2,2-trifluoroethyl) ethylphosphonate as novel high-efficient flame retardant additive for safer lithium-ion battery. *Electrochim. Acta* **2015**, *165*, 67–71.

[44] Liu, K.; Liu, W.; Qiu, Y. C.; Kong, B.; Sun, Y. M.; Chen, Z.; Zhuo, D.; Lin, D. C.; Cui, Y. Electrospun core–shell microfiber separator with thermal-triggered flame-retardant properties for lithium-ion batteries. *Sci. Adv.* **2017**, *3*, e1601978.

[45] Kim, J. H.; Kim, J. H.; Kim, J. M.; Lee, Y. G.; Lee, S. Y. Superlattice crystals-mimic, flexible/functional ceramic membranes: Beyond polymeric battery separators. *Adv. Energy Mater.* **2015**, *5*, 1500954.

[46] Kang, S. M.; Ryou, M. H.; Choi, J. W.; Lee, H. Mussel-and diatom-inspired silica coating on separators yields improved power and safety in Li-ion batteries. *Chem. Mater.* **2012**, *24*, 3481–3485.

[47] Van der Veen, I.; de Boer, J. Phosphorus flame retardants: Properties, production, environmental occurrence, toxicity and analysis. *Chemosphere* **2012**, *88*, 1119–1153.

[48] Green, J. A review of phosphorus-containing flame retardants. *J. Fire Flammabl.* **1992**, *10*, 470–487.